

✦ FLAIR: Frequency- and Locality-Aware Implicit Neural Representations

Sukhun Ko¹, Dahyeon Kye¹, Kyle Min², Chanho Eom¹, Jihyong Oh^{1†}

¹Chung-Ang University, South Korea ²Intel Labs, USA
{l00l00330, rpek9us, cheom, jihyongoh}@cau.ac.kr, kyle.min@intel.com

<https://cmlab-korea.github.io/FLAIR/>

Abstract

Implicit Neural Representations (INRs) leverage neural networks to map coordinates to corresponding signals, enabling continuous and compact representations. This paradigm has driven significant advances in various vision tasks. However, existing INRs lack frequency selectivity, spatial localization, and sparse representations, leading to an over-reliance on redundant signal components. Consequently, they exhibit spectral bias, tending to learn low-frequency components early while struggling to capture fine high-frequency details. To address these issues, we propose FLAIR (Frequency- and Locality-Aware Implicit Neural Representations), which incorporates two key innovations. The first is RC-GAUSS, a novel activation designed for explicit frequency selection and spatial localization under the constraints of the time-frequency uncertainty principle (TFUP). The second is Wavelet-Energy-Guided Encoding (WEGE), which leverages the discrete wavelet transform (DWT) to compute energy scores and explicitly guide frequency information to the network. Our method consistently outperforms existing INRs in 2D image representation and restoration, as well as 3D reconstruction. Please visit our project page at <https://cmlab-korea.github.io/FLAIR/>.

1 Introduction

Traditional representations, including discrete grid-based methods (Choy et al. 2016) such as volumes and unstructured formats like point clouds, have contributed to solving various vision problems (Tewari et al. 2022). However, these approaches have increasingly shown limitations in addressing the diverse and ill-posed inverse problems (Demoment 2002). To overcome these limitations, implicit neural representations (INRs) (Sitzmann et al. 2020) model signals as continuous mappings from input coordinates to their corresponding values via neural networks, thereby supporting continuous attribute queries and facilitating the seamless integration of differentiable physical processes. This coordinate-based paradigm has enabled notable advances in previously challenging tasks such as super-resolution (SR) (Chen, Liu, and Wang 2021) and denoising (Buades, Coll, and Morel 2005). More recently, it has been extended to complex, higher-dimensional problems including 3D oc-

cupancy estimation (Mescheder et al. 2019) and neural radiance fields (NeRF) (Mildenhall et al. 2021).

However, existing INR methods commonly suffer from the spectral bias problem (Rahaman et al. 2019), where networks tend to learn low-frequency components first. This leads to an inability to recover fine details, a challenge that remains unresolved. To mitigate the spectral bias, various positional encoding (PE) schemes have been proposed, such as Sinusoidal PE (Tancik et al. 2020) and Wavelet PE (Zhao et al. 2025), which embed input coordinates into a higher-dimensional space using a fixed set of basis functions. Although these approaches embed coordinate information into a fixed set of M bases, their representational capacity is fundamentally limited by the number of bases M , as well as by their learnable range. These limitations hinder their ability to solve inverse problems and often result in imperfect representations (Rahimi and Recht 2007).

Beyond predefined frequency bases, recent studies (Sitzmann et al. 2020; Serrano, Szymkowiak, and Musialski 2024) have attempted to mitigate spectral bias by enhancing the expressiveness of activation functions. However, these methods have primarily focused on broadening the domain of activation functions (Liu et al. 2024), rather than enabling precise frequency selection. As a result, networks may construct redundant or overlapping bases, lacking the ability to selectively target the necessary frequency bands. This limitation impairs their effectiveness in real-world inverse problems, such as denoising (Yan, Liu, and Li 2024), where the suppression of irrelevant frequency bands (*e.g.*, noise) is essential for accurate signal recovery.

To address these limitations, we propose **FLAIR** (frequency- and locality-aware implicit neural representations), which serves as a unified architecture integrating two complementary components: (i) RC-GAUSS (Sec. 3.3) for frequency-domain selection and time-domain localization, and (ii) Wavelet-Energy-Guided Encoding (WEGE) (Sec. 3.5) for region-adaptive frequency guidance.

Specifically, we adopt a band-limited function that enables explicit frequency selection for signal modeling. However, increasing the degree of band-limitation inevitably induces oscillations in the time domain, causing training instability and degraded time-domain localization (Gottlieb and Shu 1997). Therefore, instead of using the ideal band-limited function, *sinc* (Saratchandran et al. 2024), we base

[†]Corresponding author

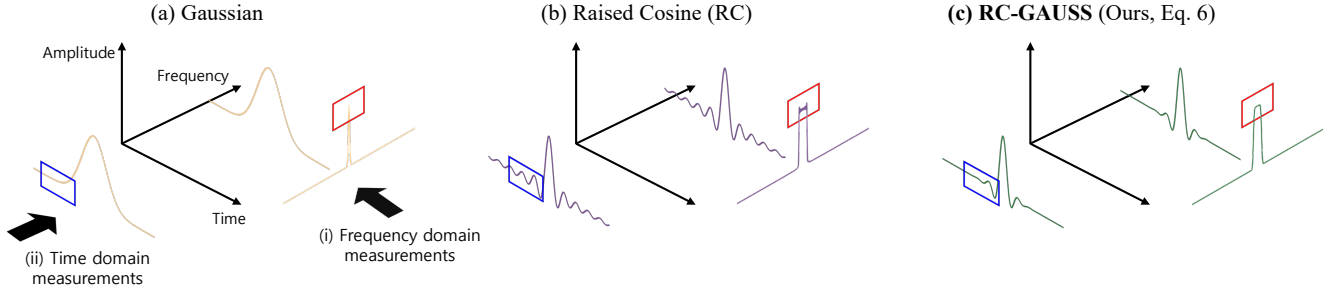


Figure 1: **Our RC-GAUSS (c) achieves both precise frequency selection and time localization under the TFUP, as compared to Gaussian (a) and RC (b).** RC-GAUSS (c), as a core component of FLAIR, integrates RC (b) for band-limited frequency selectivity with a Gaussian (a) envelope for time localization. (i) *Frequency-domain comparison*: RC (b), a typical band-limited function, achieves sharper frequency selectivity than Gaussian-based functions (a) and (c). It resembles an ideal rectangular pulse but suffers from ripples due to discrete sampling (red box in (b)), potentially causing artifacts. In contrast, RC-GAUSS (c) offers slightly lower frequency selectivity but reduces ripples, thereby mitigating artifacts. (ii) *Time-domain comparison*: RC-GAUSS (c), as highlighted by the blue box in (c), effectively suppresses the infinite oscillations inherent in RC (b) by applying a Gaussian (a) envelope, thereby reducing unstable training. For clarity, only a single basis function is illustrated. In practice, INRs represent signals through the composition of multiple bases.

our design on the *raised cosine* (RC) (Kekre, Sahasrabudhe, and Goyal 1983) function to improve training stability. Furthermore, we introduce a Gaussian envelope (Ramasinghe and Lucey 2022) to suppress residual oscillations, resulting in the proposed **RC-GAUSS** function (Fig. 1(c)), which multiplies an RC function (Fig. 1(b)) by a Gaussian (Fig. 1(a)), as highlighted by the blue boxes. Although the time–frequency uncertainty principle (TFUP) (Gröchenig 2001) states that perfect localization in both domains is unattainable, our formulation allows the model to adaptively learn the optimal trade-off for each task via learnable parameters. Note that the time (temporal) domain corresponds to the spatial domain in images.

As the second key component of FLAIR, we propose **Wavelet-Energy-Guided Encoding (WEGE)** (Sec. 3.5), which adaptively provides explicit information to quantify continuous-frequency components, indicating whether a region is high- or low-frequency. This allows the model to perform region-adaptive frequency selection, thereby enhancing its representational flexibility. Notably, WEGE requires only 0.1k additional parameters and is compatible with plug-and-play integration into other activation-based architectures. In particular, it complements RC-GAUSS by providing explicit frequency information that enhances its frequency selection capability.

We validate the effectiveness of FLAIR and its components, RC-GAUSS and WEGE, across a variety of experiments and applications. Our approach demonstrates superiority not only in 2D image fitting and restoration, as shown in Fig. 2, but also in 3D representation tasks. In summary, our main contributions are as follows:

- We propose FLAIR, a unified architecture that integrates two complementary components: (i) RC-GAUSS, a band-limited nonlinear activation that jointly enables frequency-domain selection and time-domain localiza-

tion, and (ii) Wavelet-Energy-Guided Encoding (WEGE) for region-adaptive frequency guidance.

- We introduce RC-GAUSS, a novel nonlinear activation that mitigates spectral bias through the frequency selection ability of the *raised cosine* (RC) function, while suppressing oscillations and enhancing time localization through the Gaussian envelope.
- We propose WEGE, which provides explicit information that quantifies continuous-frequency components as input, allowing the activation function to perform frequency selection in a region-adaptive manner.

2 Related Work

2.1 Implicit Neural Representations

Standard MLPs with ReLU activations exhibit a strong bias towards learning low-frequency content due to the non-periodic nature of ReLU, limiting their ability to capture fine details, a phenomenon known as spectral bias (Rahaman et al. 2019). To address this spectral bias (Cai et al. 2024), a series of periodic activation functions have been proposed, most notably SIREN (Sitzmann et al. 2020) and FINER (Liu et al. 2024). SIREN employs sinusoidal activations to model high-frequency components, but its performance is highly dependent on the choice of hyperparameters and is sensitive to initialization, necessitating careful design choices to avoid suboptimal results. FINER introduces a variable-periodic sine activation and tunes the supported frequency set by adjusting the initialization range of the bias vector. However, in practice, both SIREN and FINER remain limited in addressing the spectral bias problem due to the inherent constraints of periodic activations.

Alternatively, wavelet-based activations such as WIRE (Saragadam et al. 2023) have aimed to address spectral bias through spatial localization and compactness,

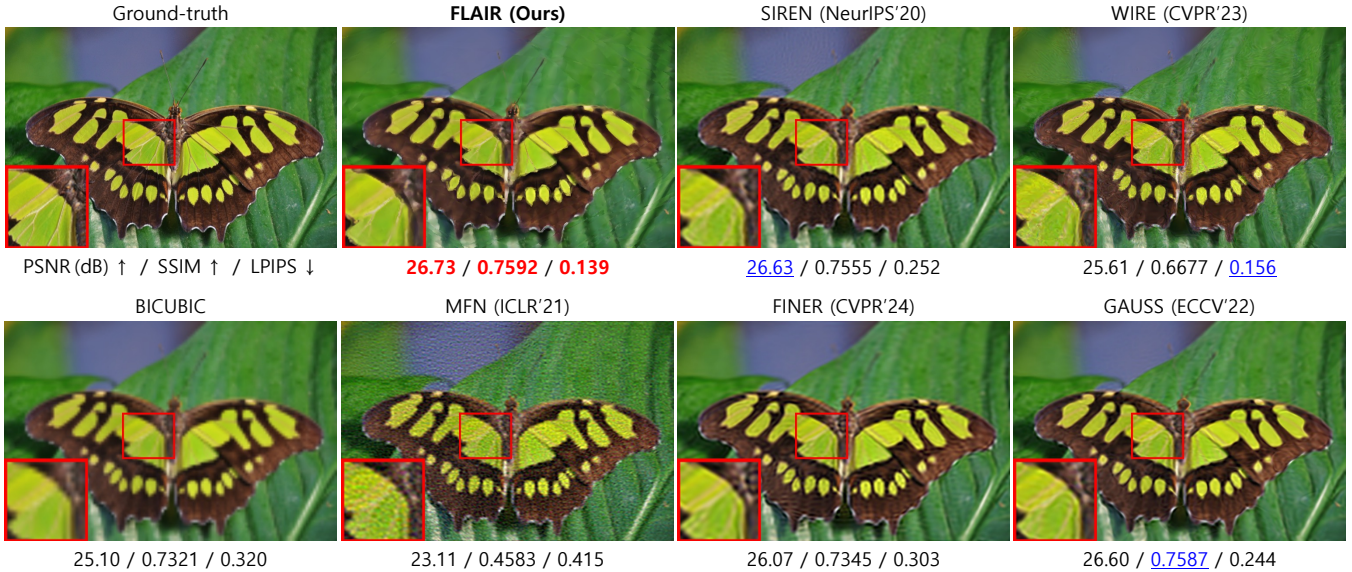


Figure 2: **Image fine-detail reconstruction capabilities of FLAIR on $\times 4$ image super-resolution.** As shown in the red box, other nonlinear activations exhibit undesired frequency leakage, whereas FLAIR accurately selects target frequencies, achieving the best performance in all metrics, most notably in LPIPS. **Red** (bold) and **blue** (underlined) denote the best and second-best performances, respectively. *Best viewed in zoom.*

offering improved interpretability and spatial control. Nonetheless, these approaches remain limited in their ability to fully overcome spectral bias, as they do not offer explicit frequency selection.

More recently, filter-based activation functions have been actively investigated in the context of INRs. A recent theoretical analysis (Saratchandran et al. 2024) has suggested that sinc functions, as a type of filter-based activation, can serve as an optimal choice for INR tasks. Despite their theoretical advantages, these filter-based functions exhibit inherent limitations. In the spatial domain, their infinite oscillations can induce training instability and visual artifacts, and as a result, empirical validation of their effectiveness across diverse vision tasks remains limited.

To address these challenges, we propose RC-GAUSS, a key component of FLAIR that enables joint spatial localization and frequency selection. By operating under the TFUP, RC-GAUSS allows the model to adaptively balance spatial localization and frequency selectivity during training, thereby mitigating spectral bias and overcoming the aforementioned limitations.

2.2 Frequency-Guided Representations and Conditioning

Frequency-guided representations and conditioning methods have been actively explored to enhance the modeling of task-relevant frequency components, which are essential for preserving fine details in low-level vision tasks (Li et al. 2023; Wang et al. 2024). For example, Local Texture Estimator for Implicit Representation Function (LTE) (Lee and Jin 2022) employs dedicated modules composed of convolutional neural networks (CNN) (Krizhevsky, Sutskever,

and Hinton 2012) and fully connected (FC) layers (Basha et al. 2020) to separately estimate key frequency components, such as amplitude, frequency, and phase, allowing the network to infer dominant frequencies and the corresponding Fourier coefficients.

In parallel, the Local Implicit Wavelet Transformer (LIWT) (Duan et al. 2024) leverages DWT to decompose input features into low- and high-frequency components, which are further refined to enhance frequency-aware representation. More recently, Zhao et al. (2025) introduce a method that adaptively places local wavelet bases at high-frequency regions, enabling efficient encoding of fine details (Zhao et al. 2025).

Building on this line of research, we propose a novel encoding, WEGE (Sec. 3.5), specifically designed to work with activation functions in INRs. Unlike other approaches that rely on additional auxiliary networks, which often result in slow convergence, our method explicitly assigns DWT-based energy scores to each coordinate, enabling region-adaptive frequency selection and improved performance.

3 Proposed Method: FLAIR

In this section, we first explain the time–frequency uncertainty principle (TFUP), which forms the theoretical basis of our approach. We then provide a brief formulation of an Implicit Neural Representation (INR). Building on these foundations, we present a novel framework, FLAIR, composed of two key components: (i) RC-GAUSS, a band-limited nonlinear activation for frequency-domain selection and time-domain localization, and (ii) Wavelet-Energy-Guided Encoding (WEGE) for region-adaptive frequency guidance.

3.1 Preliminary: Time-Frequency Uncertainty Principle

The mathematical foundation of the time-frequency uncertainty principle (TFUP) in signal processing originates from the Heisenberg uncertainty principle (Busch, Heinonen, and Lahti 2007) in quantum mechanics, which states that there is a fundamental limit to simultaneously and precisely measuring a particle’s position and momentum:

$$\Delta x \cdot \Delta p \geq \frac{\hbar}{2}, \text{ where } \hbar = \frac{h}{2\pi}, \quad (1)$$

where Δx is the standard deviation of position, Δp is the standard deviation of momentum, and h is Planck’s constant.

Extending this concept to the domain of signal processing (Parhizkar, Barbotin, and Vetterli 2015), the TFUP states that for any signal $x(t)$, the product of its temporal standard deviation σ_t and frequency standard deviation σ_f is bounded below by

$$\sigma_t \sigma_f \geq \frac{1}{4\pi}, \quad (2)$$

where σ_t and σ_f quantify the temporal and frequency uncertainty of $x(t)$, respectively. This relationship implies that a signal highly localized in time (small σ_t) must necessarily have a broad frequency spectrum (large σ_f), and vice versa. Thus, the uncertainty principle imposes a fundamental limit on the simultaneous localization of a signal in both time and frequency domains.

3.2 Formulation of an INR

An Implicit Neural Representation (INR) aims to represent a continuous signal by directly mapping input coordinates to their corresponding signal values through a neural network F_θ . Formally, the function is defined as:

$$F_\theta : \mathbb{R}^{d_{in}} \rightarrow \mathbb{R}^{d_{out}}, \quad \mathbf{x} \mapsto F_\theta(\mathbf{x}), \quad (3)$$

where $\theta \in \mathbb{R}^M$ denotes all learnable parameters of the network. The input $\mathbf{x} \in \mathbb{R}^{d_{in}}$ corresponds to a spatial coordinate (e.g., (x, y) for 2D or (x, y, z) for 3D), and the output $F_\theta(\mathbf{x}) \in \mathbb{R}^{d_{out}}$ represents the signal value at that location (e.g., RGB color or occupancy value). The training data is given as a set of pairs:

$$\mathcal{D} = \{(\mathbf{x}_i, \mathbf{y}_i)\}_{i=1}^N, \quad (4)$$

where \mathbf{y}_i denotes the ground-truth signal at coordinate \mathbf{x}_i . The network is optimized by minimizing a standard mean squared error (MSE) loss:

$$\mathcal{L}(\theta) = \frac{1}{N} \sum_{i=1}^N \|F_\theta(\mathbf{x}_i) - \mathbf{y}_i\|_2^2, \quad (5)$$

where N denotes the number of training samples. This simple yet general formulation enables INRs to model complex signals with high fidelity. However, achieving accurate reconstruction of visual signals requires stronger control over both frequency selection and spatial localization. To address this, we further optimize F_θ by introducing a nonlinear function RC-GAUSS that achieves these properties.

3.3 Proposed RC-GAUSS Function

As shown in Fig. 1(c) red box, RC-GAUSS exploits the sharp cut-off behavior of RC for frequency selectivity while suppressing infinite oscillations (blue box) through a Gaussian envelope, thereby enabling improved time localization. Formally, RC-GAUSS is expressed as a modulated basis function:

$$\psi_x^{\text{RC-GAUSS}} = \phi_x^{\text{basis}} \cdot \exp(2\pi\zeta xj), \quad (6)$$

where ζ denotes the modulation frequency, and j is the imaginary unit. Note that all the above functions are defined in the time domain. Importantly, multiplying by $\exp(2\pi\zeta xj)$ in the time domain is equivalent to shifting the frequency support of the basis function to ζ in the Fourier domain. This allows the basis to be centered at any desired frequency, enabling the network to adaptively capture both low- and high-frequency components as needed. In practice, ζ is treated as a learnable parameter. The basis function ϕ_x^{basis} is defined as:

$$\phi_x^{\text{basis}} = \frac{\text{sinc}\left(\frac{x}{T}\right)}{T} \cdot \frac{\cos(\pi\beta x/T)}{1 - (2\beta x/T)^2} \cdot \exp\left(-\frac{x^2}{2\sigma^2}\right), \quad (7)$$

where T is the bandlimit parameter controlling the overall bandwidth and is treated as a learnable parameter, β is the roll-off factor of the raised cosine term, fixed at 0.05 to preserve the inherent sharpness of the band-limited cutoff, and σ is the standard deviation of the Gaussian envelope, also treated as a learnable parameter to adaptively govern spatial localization.

We employ this function as the activation in each layer of our implicit neural representation (INR) network:

$$\begin{aligned} \bar{z}^0 &= \bar{x}, \\ \bar{z}^l &= \psi_x(W^l \bar{z}^{l-1} + \bar{b}^l), \quad l = 1, 2, \dots, L-1, \\ f(\bar{x}; \theta) &= W^L \bar{z}^{L-1} + \bar{b}^L. \end{aligned} \quad (8)$$

\bar{x} denotes the input coordinate to the network and $\psi_x(\cdot)$ is our proposed nonlinear function, RC-GAUSS. \bar{z}^l indicates the output of layer l . L denotes the total number of layers in the network, $\theta = \{W^l, \bar{b}^l \mid l = 1, \dots, L\}$ denotes the set of learnable parameters. This structure enables each layer to adaptively exploit both frequency selectivity and spatial localization, resulting in a more expressive INR.

3.4 Neural Tangent Kernel Perspective

Neural Tangent Kernel (NTK) theory (Jacot, Gabriel, and Hongler 2018) provides a principled framework to interpret neural network training as kernel regression. The convergence dynamics are fundamentally governed by the distribution of NTK eigenvalues, where larger eigenvalues correspond to components that are learned more rapidly and thus fitted more accurately (Bai et al. 2023).

Following FINER (Liu et al. 2024), we consider a simple 1D input-output case formulated as $f(x; \theta) = \sum_{k=1}^n c_k \sigma(w_k x + b_k)$, where $c_k \in \mathbb{R}$ are output weights

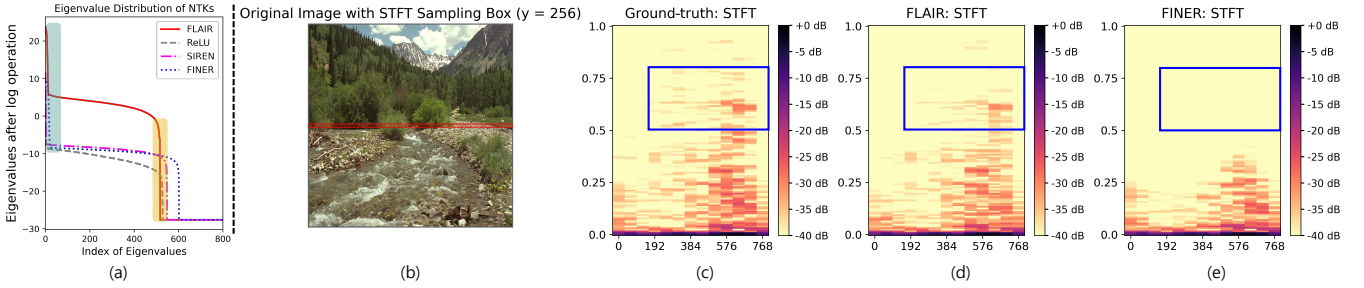


Figure 3: **Eigenvalue distribution of NTKs (a) and Short-time Fourier Transform (STFT) results (b)–(e).** In (a), FLAIR (ours) shows exceptionally high eigenvalues (green box) and a sharp cut-off (yellow box), indicating its band-limited structure. In (b), original image with a horizontal 1D scan line ($y = 256$, red) used for STFT. STFT is computed using a 256-sample Hann window with 75% overlap (hop size = 64), and the x-axis shows the window start index along the scan line. The STFT results of the ground-truth, FLAIR, and FINER are visualized in (c)–(e), respectively. The y-axis indicates normalized frequency, where higher values correspond to higher frequency components, and the colorbar shows amplitude in decibels (dB).

and $\sigma(\cdot)$ is our proposed nonlinear activation function RC-GAUSS. For two input points x and x' , the Neural Tangent Kernel (NTK) is defined as $T(x, x') = \mathbb{E}_\theta [\nabla_\theta f(x; \theta) \cdot \nabla_\theta f(x'; \theta)]$, where $\nabla_\theta f(x; \theta)$ denotes the gradient of the network output with respect to its parameters, “ \cdot ” denotes the inner product, and the expectation is taken over the random initialization of θ .

Fig. 3(a) shows the NTK eigenvalue distributions of several activations. The x-axis represents the index of eigenvalues, typically interpreted for periodic activations as being ordered from low- to high-frequency modes, and the y-axis indicates the eigenvalues, which reflect how effectively each mode can be fitted during training. FINER (Liu et al. 2024) spans the widest range of eigenvalues, alleviating spectral bias through its broad coverage of low- to high-frequency modes. In contrast, FLAIR retains exceptionally large eigenvalues concentrated in the low-index region (green box) and exhibits a sharp cut-off at higher indices (yellow box). This distribution should not be interpreted in the same way as periodic activations such as SIREN or FINER, as FLAIR is a band-limited function equipped with an intrinsic frequency-shifting mechanism. Its eigenvalue indices do not strictly follow the conventional low-to-high frequency ordering. Instead, by leveraging this mechanism, it can selectively redirect these concentrated eigenmodes to higher spectral regions when required, thereby enabling both fast convergence and accurate high-frequency detail representation despite its narrower eigenvalue spectrum. This interpretation is further supported by the short-time Fourier transform (STFT) analysis in Fig. 3. On a practical 1D line-sampled image-fitting task, STFT shows that our FLAIR (d) represents high-frequency components more effectively than FINER (e), as highlighted by the blue boxes. This confirms that FLAIR’s inherent frequency-selection and frequency-shifting capability effectively activates the necessary high-frequency components in real scenarios.

3.5 Wavelet-Energy-Guided Encoding (WEGE)

To reduce artifacts arising from improper frequency assignment in low-frequency regions and to alleviate spectral

bias by modeling only the necessary frequencies in high-frequency regions, we introduce **Wavelet-Energy-Guided Encoding (WEGE)**. WEGE adaptively provides explicit information that quantifies continuous-frequency components, effectively indicating whether each region is dominated by high- or low-frequency content.

Our method first computes a pixel-wise energy score E_b for each spatial coordinate (x, y) of the input image by applying the discrete wavelet transform (DWT). Formally, we decompose the input image I_k into high- and low-frequency components via DWT and compute E_b as:

$$D_k^H, D_k^L = \text{DWT}(I_k), \quad (9)$$

$$E_b = \text{IDWT}(D_k^H) - \text{IDWT}(D_k^L).$$

The components of D_k^H correspond to the high-frequency sub-bands $\{HL, LH, HH\}$, while D_k^L corresponds to the low-frequency sub-band $\{LL\}$. E_b is a pixel-wise energy score map that adaptively highlights high-frequency structures such as edges and textures. Its normalized form, w_b , is defined as follows:

$$w_b = \frac{E_b - E_{\min}}{E_{\max} - E_{\min} + \epsilon}, \quad (10)$$

where E_{\min} and E_{\max} denote the minimum and maximum energy values within the image, respectively, and ϵ is a small constant for numerical stability.

Although the w_b -based normalized energy score map exhibits edge-aware properties, pixel-wise scoring often results in discontinuities, consequently producing visually noisy artifacts in the RGB output domain. To address this, we apply a filtering operation to the normalized scores in order to suppress such score discontinuities.

Among various filtering methods, the guided filter (He, Sun, and Tang 2012) demonstrated the best performance, as detailed in the supplemental material. Accordingly, the guided filtering operation \mathcal{G} is applied to the normalized energy score map to mitigate discontinuities while preserving edge structures, formulated as:

$$\tilde{w}_b(x) = \mathcal{G}(I(x), w_b(x); r, \epsilon), \quad (11)$$

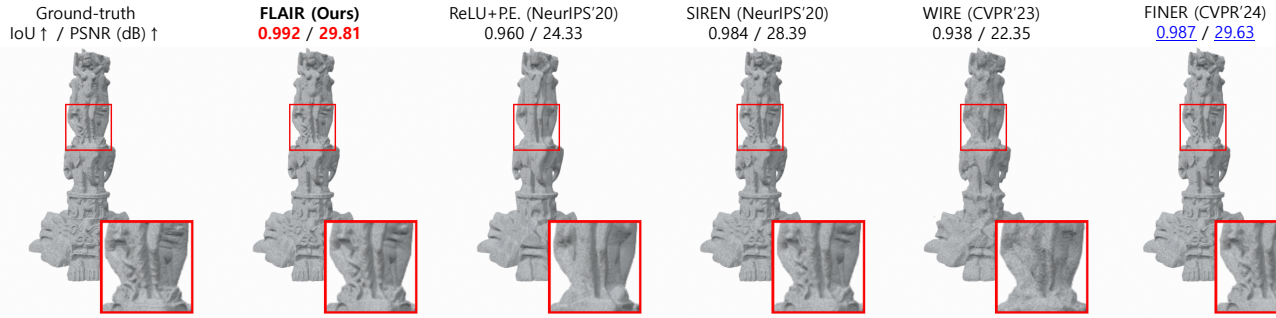


Figure 4: **Visual comparisons for occupancy field representations.** The results show that FLAIR achieves the highest IoU and PSNR while preserving the finest details. *Best viewed in zoom.*

where $I(x)$ is the gray-scale guidance input image, $w_b(x)$ is the normalized wavelet energy score at pixel x , r is the window radius, and ϵ is the regularization parameter.

The resulting filtered energy score map \tilde{w}_b , obtained by applying the guided filtering in Eq. (11), is concatenated with the original spatial coordinates (x, y) and fed as input to the INR network:

$$S(x, y) = f_\theta(x, y, \tilde{w}_b), \quad (12)$$

where f_θ denotes the INR network parameterized by θ , which internally employs the proposed nonlinear activation RC-GAUSS to adaptively select frequencies based on the local characteristics inferred from WEGE. This frequency-aware modulation enables precise characterization and reconstruction of each region of the target signal, capturing both high-frequency details and low-frequency structures.

4 Experiments

Implementation Details. We thoroughly explore all possible combinations of learning rates (1×10^{-2} , 5×10^{-3} , 1×10^{-3} , 5×10^{-4} , 1×10^{-4}) for each of the state-of-the-art (SOTA) models to choose each best model for fair comparisons. For our model, we used a learning rate of 5×10^{-4} in all experiments. For activation functions that are sensitive to initialization, such as SIREN (where the initial ω_0 is set to a large value, e.g., 30), we followed each method’s recommended setting whenever available. For our FLAIR, the initialization strategy for the parameters T, β, ζ, σ is detailed in the *Supplementary*. All models were trained with 4 hidden layers and 256 hidden features per layer, and the number of training iterations was kept consistent across all models. All experiments were conducted on an RTX A6000 GPU.

Datasets. We conduct 2D experiments on the DIV2K (Agustsson and Timofte 2017) and Kodak datasets (E.Kodak 1999), both of which are widely recognized benchmarks for image reconstruction and representation learning. For 3D experiments, we employ the Stanford 3D Scanning Repository (Stanford University Computer Graphics Laboratory 1994), a standard benchmark commonly used for evaluating implicit neural representation methods.

Metrics. For comprehensive quantitative evaluations, we evaluate each method using standard image quality met-

Table 1: **Comparison of different methods with model parameters.** Quantitative results on the Kodak dataset (24 images), reported in PSNR (dB), SSIM, and LPIPS. **Bold** and underlined values indicate the best and second-best performances, respectively.

Methods	#Params (K)↓	PSNR↑	SSIM↑	LPIPS↓
FINER (CVPR’24)	198.9	<u>30.11</u>	<u>0.8227</u>	<u>0.300</u>
WIRE (CVPR’23)	91.6	28.80	0.7928	0.333
SIREN (NeurIPS’20)	198.9	28.47	0.7709	0.382
GAUSS (ECCV’22)	198.9	27.30	0.7278	0.444
ReLU+P.E. (NeurIPS’20)	204.0	21.80	0.5447	0.737
FLAIR (Ours)	199.0	30.13	0.8506	0.225

rics, including PSNR, Structural Similarity Index Measure (SSIM) (Wang et al. 2004), and Learned Perceptual Image Patch Similarity (LPIPS) (Zhang et al. 2018), to evaluate the fidelity and perceptual quality of the reconstructed images.

4.1 Signal Representation

As one of the key capabilities of INRs is the representation of signals, we evaluate two tasks in this experiment: 2D image representation and 3D occupancy volume prediction.

2D Image Representation. For the 2D image representation task, we use the widely adopted Kodak dataset and conduct experiments on all 24 images. Results after 5,000 training epochs are summarized in Table 1. As shown in Table 1, our model achieves the best average scores across all metrics, with notably superior LPIPS performance, which we attribute to the strong frequency selection capability of our filter-based activation function. Comprehensive per-scene qualitative results and detailed quantitative metrics are provided in the *Supplementary*.

3D Occupancy Volume Prediction. For the 3D occupancy volume prediction task (Mescheder et al. 2019), we follow the standard protocol by constructing occupancy volumes through point sampling on a $512 \times 512 \times 512$ grid, assigning 1 to voxels inside the object and 0 otherwise. As shown in Fig. 4, FLAIR consistently achieves higher IoU and PSNR scores compared to other methods and delivers significantly more fine-grained and accurate reconstructions of 3D shapes.

Table 2: **Arbitrary-scale super-resolution comparison.** Quantitative results on the Kodak dataset at $\times 6$ and $\times 8$ up-scaling. **Bold** and underlined values indicate the best and second-best scores, respectively.

Methods	$\times 6$			$\times 8$		
	PSNR \uparrow	SSIM \uparrow	LPIPS \downarrow	PSNR \uparrow	SSIM \uparrow	LPIPS \downarrow
FINER (CVPR'24)	23.94	0.6495	0.425	22.57	0.5761	0.549
WIRE (CVPR'23)	22.29	0.4770	<u>0.273</u>	19.12	0.3191	<u>0.392</u>
GAUSS (ECCV'22)	<u>24.24</u>	<u>0.6601</u>	0.382	<u>22.84</u>	<u>0.6051</u>	0.492
MFN (ICLR'21)	20.64	0.3066	0.594	18.93	0.5761	0.667
SIREN (NeurIPS'20)	24.18	0.6568	0.384	22.84	0.5801	0.443
ReLU+P.E. (NeurIPS'20)	22.51	0.6073	0.398	21.85	0.5870	0.415
FLAIR (Ours)	24.32	0.6625	0.226	23.15	0.6097	0.329

Table 3: **Ablation study of layer-wise learned parameters in RC-GAUSS, showing adaptation to scene complexity.**

Scene	Layer (l)	T	σ	ζ
Complex (Kodak 08)	1	0.711	1.956	0.276
	2	1.025	2.009	0.106
	3	1.045	2.040	0.092
	4	0.675	1.466	0.267
	Average	0.864	1.868	0.185
Homogeneous (Kodak 16)	1	1.034	1.966	0.215
	2	1.025	2.019	0.098
	3	0.963	2.140	0.088
	4	1.007	2.012	0.120
	Average	1.005	2.015	0.130

4.2 Inverse Problems of 2D Images

Arbitrary-Scale Super-Resolution. INRs inherently act as continuous interpolants, enabling super-resolution beyond fixed scales. Accordingly, we evaluate our method under arbitrary-scale scenarios (*e.g.*, $\times 4$, $\times 6$, $\times 8$) on the DIV2K dataset to demonstrate its capability for continuous-scale image reconstruction. As shown in Fig. 2, our method, FLAIR, achieves the most fine-grained reconstruction at $\times 4$, as highlighted in the butterfly’s wings (red box). Furthermore, as reported in Table 2, our method consistently outperforms others at challenging scales ($\times 6$ and $\times 8$) across all metrics, particularly in perceptual quality and LPIPS.

Image Denoising. Following previous work WIRE (Saragadam et al. 2023), we evaluate our method on the image denoising task using both Poisson noise (30.0) and Gaussian noise (2.0). Denoising is a particularly challenging problem that requires not only effective noise suppression but also the preservation of fine details. To address this challenge, precise frequency selection at the exact locations where noise and image structures interact is essential. Our approach is specifically designed to meet this requirement, and as shown in our comparison results provided in the *Supplementary*, it achieves superior performance by selectively recovering details while effectively removing noise.

4.3 Ablation Study

To validate whether the learnable parameters of RC-GAUSS adapt to scene complexity and dominant frequency characteristics, we conduct an image fitting experiment on two

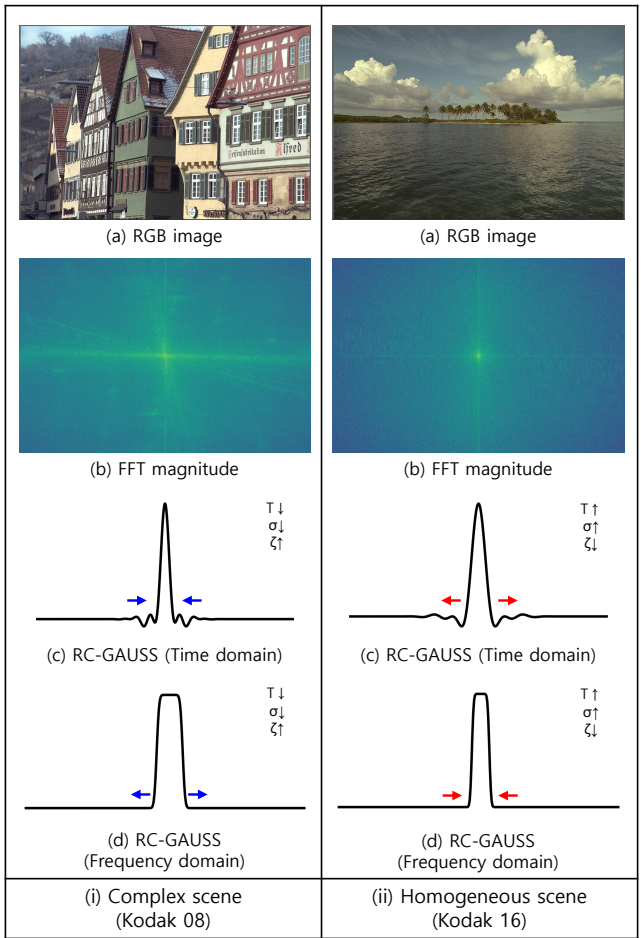


Figure 5: **Ablation study on scene adaptivity.** Visualization of (i) complex and (ii) homogeneous scenes, each consisting of (a) an RGB image, (b) the magnitude of its Fast Fourier Transform (FFT), (c) the time-domain representation of the learned RC-GAUSS function, and (d) the corresponding frequency-domain representation.

representative scenes, (i) complex and (ii) homogeneous, as shown in Fig. 5. We fit RC-GAUSS to each image and report the learned parameters (T , σ , ζ) across layers in Table 3. In Table 3, the complex scene (Kodak 08) exhibits smaller average values of T and σ , indicating stronger temporal localization and broader frequency-domain support, as reflected in Fig. 5(i)(c) and (d). The elevated ζ value leads to a spectral shift observed in Fig. 5(i)(d), indicating increased emphasis on high-frequency content. Further analyses of our several components are provided in the *Supplementary*.

5 Conclusion

We have proposed FLAIR, a Frequency- and Locality-Aware Implicit Neural Representation framework that unifies two complementary components. RC-GAUSS is a novel activation function enabling precise frequency selection while suppressing excessive spatial oscillations, thereby facilitating effective signal modeling. Wavelet-Energy-Guided

Encoding (WEGE) is a lightweight module tailored to INR architectures and RC-GAUSS, adding only 0.1k parameters. Our method consistently alleviates spectral bias and demonstrates superior fine-detail reconstruction across various tasks.

References

- Agustsson, E.; and Timofte, R. 2017. Ntire 2017 challenge on single image super-resolution: Dataset and study. In *Proceedings of the IEEE conference on computer vision and pattern recognition workshops*, 126–135.
- Bai, J.; Liu, G.-R.; Gupta, A.; Alzubaidi, L.; Feng, X.-Q.; and Gu, Y. 2023. Physics-informed radial basis network (PIRBN): A local approximating neural network for solving nonlinear partial differential equations. *Computer Methods in Applied Mechanics and Engineering*, 415: 116290.
- Basha, S. S.; Dubey, S. R.; Pulabaigari, V.; and Mukherjee, S. 2020. Impact of fully connected layers on performance of convolutional neural networks for image classification. *Neurocomputing*, 378: 112–119.
- Buades, A.; Coll, B.; and Morel, J.-M. 2005. A review of image denoising algorithms, with a new one. *Multiscale modeling & simulation*, 4(2): 490–530.
- Busch, P.; Heinonen, T.; and Lahti, P. 2007. Heisenberg’s uncertainty principle. *Physics reports*, 452(6): 155–176.
- Cai, Z.; Zhu, H.; Shen, Q.; Wang, X.; and Cao, X. 2024. Batch normalization alleviates the spectral bias in coordinate networks. In *Proceedings of the IEEE/CVF conference on computer vision and pattern recognition*, 25160–25171.
- Chen, Y.; Liu, S.; and Wang, X. 2021. Learning continuous image representation with local implicit image function. In *Proceedings of the IEEE/CVF conference on computer vision and pattern recognition*, 8628–8638.
- Choy, C. B.; Xu, D.; Gwak, J.; Chen, K.; and Savarese, S. 2016. 3d-r2n2: A unified approach for single and multi-view 3d object reconstruction. In *European conference on computer vision*, 628–644. Springer.
- Demoment, G. 2002. Image reconstruction and restoration: Overview of common estimation structures and problems. *IEEE Transactions on Acoustics, Speech, and Signal Processing*, 37(12): 2024–2036.
- Duan, M.; Qu, L.; Liu, S.; and Wang, M. 2024. Local implicit wavelet transformer for arbitrary-scale super-resolution. *arXiv preprint arXiv:2411.06442*.
- E.Kodak. 1999. Kodak Lossless True Color Image Suite. <https://r0k.us/graphics/kodak/>. Accessed: June 1, 2025.
- Gottlieb, D.; and Shu, C.-W. 1997. On the Gibbs phenomenon and its resolution. *SIAM review*, 39(4): 644–668.
- Gröchenig, K. 2001. *Foundations of time-frequency analysis*. Springer Science & Business Media.
- He, K.; Sun, J.; and Tang, X. 2012. Guided image filtering. *IEEE transactions on pattern analysis and machine intelligence*, 35(6): 1397–1409.
- Jacot, A.; Gabriel, F.; and Hongler, C. 2018. Neural tangent kernel: Convergence and generalization in neural networks. *Advances in neural information processing systems*, 31.
- Kekre, H.; Sahasrabudhe, S.; and Goyal, N. 1983. Raised cosine function for image restoration. *Signal Processing*, 5(1): 61–73.
- Koneputugodage, C. H.; Ben-Shabat, Y.; Ramasinghe, S.; and Gould, S. 2025. VI³NR: Variance Informed Initialization for Implicit Neural Representations. In *Proceedings of the Computer Vision and Pattern Recognition Conference*, 13477–13486.
- Krizhevsky, A.; Sutskever, I.; and Hinton, G. E. 2012. Imagenet classification with deep convolutional neural networks. *Advances in neural information processing systems*, 25.
- Lee, J.; and Jin, K. H. 2022. Local texture estimator for implicit representation function. In *Proceedings of the IEEE/CVF conference on computer vision and pattern recognition*, 1929–1938.
- Li, F.; Zhang, L.; Liu, Z.; Lei, J.; and Li, Z. 2023. Multi-frequency representation enhancement with privilege information for video super-resolution. In *Proceedings of the IEEE/CVF international conference on computer vision*, 12814–12825.
- Liu, Z.; Zhu, H.; Zhang, Q.; Fu, J.; Deng, W.; Ma, Z.; Guo, Y.; and Cao, X. 2024. Finer: Flexible spectral-bias tuning in implicit neural representation by variable-periodic activation functions. In *Proceedings of the IEEE/CVF Conference on Computer Vision and Pattern Recognition*, 2713–2722.
- Mescheder, L.; Oechsle, M.; Niemeyer, M.; Nowozin, S.; and Geiger, A. 2019. Occupancy networks: Learning 3d reconstruction in function space. In *Proceedings of the IEEE/CVF conference on computer vision and pattern recognition*, 4460–4470.
- Mildenhall, B.; Srinivasan, P. P.; Tancik, M.; Barron, J. T.; Ramamoorthi, R.; and Ng, R. 2021. NeRF: Representing scenes as neural radiance fields for view synthesis. *Communications of the ACM*, 65(1): 99–106.
- Parhizkar, R.; Barbotin, Y.; and Vetterli, M. 2015. Sequences with minimal time–frequency uncertainty. *Applied and computational harmonic analysis*, 38(3): 452–468.
- Rahaman, N.; Baratin, A.; Arpit, D.; Draxler, F.; Lin, M.; Hamprecht, F.; Bengio, Y.; and Courville, A. 2019. On the spectral bias of neural networks. In *International conference on machine learning*, 5301–5310. PMLR.
- Rahimi, A.; and Recht, B. 2007. Random features for large-scale kernel machines. *Advances in neural information processing systems*, 20.
- Ramasinghe, S.; and Lucey, S. 2022. Beyond periodicity: Towards a unifying framework for activations in coordinate-mlps. In *European Conference on Computer Vision*, 142–158. Springer.
- Saragadam, V.; LeJeune, D.; Tan, J.; Balakrishnan, G.; Veer-araghavan, A.; and Baraniuk, R. G. 2023. Wire: Wavelet implicit neural representations. In *Proceedings of the IEEE/CVF Conference on Computer Vision and Pattern Recognition*, 18507–18516.
- Saratchandran, H.; Ramasinghe, S.; Shevchenko, V.; Long, A.; and Lucey, S. 2024. A sampling theory perspective

on activations for implicit neural representations. *arXiv preprint arXiv:2402.05427*.

Serrano, D.; Szymkowiak, J.; and Musialski, P. 2024. HOSC: A periodic activation function for preserving sharp features in implicit neural representations. *arXiv preprint arXiv:2401.10967*.

Sitzmann, V.; Martel, J.; Bergman, A.; Lindell, D.; and Wetzstein, G. 2020. Implicit neural representations with periodic activation functions. *Advances in neural information processing systems*, 33: 7462–7473.

Stanford University Computer Graphics Laboratory. 1994. The Stanford 3D Scanning Repository. <https://graphics.stanford.edu/data/3Dscanrep/>. Accessed: 2025-06-01.

Tancik, M.; Srinivasan, P.; Mildenhall, B.; Fridovich-Keil, S.; Raghavan, N.; Singhal, U.; Ramamoorthi, R.; Barron, J.; and Ng, R. 2020. Fourier features let networks learn high frequency functions in low dimensional domains. *Advances in neural information processing systems*, 33: 7537–7547.

Tewari, A.; Thies, J.; Mildenhall, B.; Srinivasan, P.; Treitsch, E.; Yifan, W.; Lassner, C.; Sitzmann, V.; Martin-Brualla, R.; Lombardi, S.; et al. 2022. Advances in neural rendering. In *Computer Graphics Forum*, volume 41, 703–735. Wiley Online Library.

Wang, F.; Guo, D.; Li, K.; Zhong, Z.; and Wang, M. 2024. Frequency decoupling for motion magnification via multi-level isomorphic architecture. In *Proceedings of the IEEE/CVF Conference on Computer Vision and Pattern Recognition*, 18984–18994.

Wang, Z.; Bovik, A. C.; Sheikh, H. R.; and Simoncelli, E. P. 2004. Image quality assessment: from error visibility to structural similarity. *IEEE transactions on image processing*, 13(4): 600–612.

Yan, Z.; Liu, Z.; and Li, J. 2024. Boosting of implicit neural representation-based image denoiser. In *ICASSP 2024-2024 IEEE International Conference on Acoustics, Speech and Signal Processing (ICASSP)*, 4295–4299. IEEE.

Zhang, R.; Isola, P.; Efros, A. A.; Shechtman, E.; and Wang, O. 2018. The unreasonable effectiveness of deep features as a perceptual metric. In *CVPR*, 586–595.

Zhao, H.; Gao, Z.; Wang, Y.; Xiong, R.; and Zhang, Y. 2025. Adaptive Wavelet-Positional Encoding for High-Frequency Information Learning in Implicit Neural Representation. In *Proceedings of the AAAI Conference on Artificial Intelligence*, volume 39, 10430–10438.

Supplementary Material

A Implementation Details

Initialization scheme. Proper initialization is known to be necessary for the effective training of implicit neural representations (INRs), as many activation functions require tailored initialization schemes to achieve optimal performance (Sitzmann et al. 2020). Since INR tasks demand fast convergence and stable optimization (Koneputugodage et al. 2025), we also propose an initialization scheme that reflects the characteristics of our novel activation function, RC-GAUSS, a core component of the FLAIR framework. We revisit the formulation of RC-GAUSS and provide its basis function below:

$$\psi_x^{\text{RC-GAUSS}} = \phi_x^{\text{basis}} \cdot \exp(2\pi\zeta xj), \quad (13)$$

$$\phi_x^{\text{basis}} = \frac{\text{sinc}\left(\frac{x}{T}\right)}{T} \cdot \frac{\cos(\pi\beta x/T)}{1 - (2\beta x/T)^2} \cdot \exp\left(-\frac{x^2}{2\sigma^2}\right). \quad (14)$$

The core parameters of RC-GAUSS include ζ , β , T , and σ . We begin by discussing β , which controls the transition bandwidth of the raised cosine component and influences the sharpness of its frequency response. As shown in Fig. 6, a smaller β produces a frequency response that more closely resembles an ideal rectangular filter, passing only in-band components (1) while suppressing all others (0). To preserve this band-limited behavior, we fix $\beta = 0.05$ during training, as illustrated in Fig. 6(a).

Joint initialization of T and σ for shape control. Two additional key parameters that define the RC-GAUSS function are T and σ . The parameter T governs the bandwidth of the raised-cosine component, effectively acting as a bandlimit, while σ controls the standard deviation of the Gaussian envelope. T and σ jointly determine the overall shape of the RC-GAUSS function, which makes their combination particularly important.

Under the time–frequency uncertainty principle, the ideal RC-GAUSS should exhibit strong localization in both the time and frequency domains, as illustrated in Fig. 7. We initialize $T = 1$ and $\sigma = 2$, with the function retaining the well-localized shape shown in Fig. 7. These values, however, are not fixed and can be flexibly adjusted if the localization properties are preserved. To enable task-specific adaptation, we set both T and σ as learnable so that their values can be adjusted adaptively.

Initialization of ζ for spectral control. The parameter ζ controls the modulation frequency of the basis function. In the time domain, it determines the rate at which the complex exponential $e^{2\pi j\zeta x}$ rotates in phase, effectively controlling the density of oscillations. This behavior depends on the magnitude $|\zeta|$, rather than its sign, as higher $|\zeta|$ leads to more rapid phase rotation and increased oscillation frequency, which relates to high-frequency representation, as shown in Fig. 8(i)(b). In the frequency domain, this modulation shifts the spectral support of the basis function by ζ , as shown in Fig. 8(ii)(b).

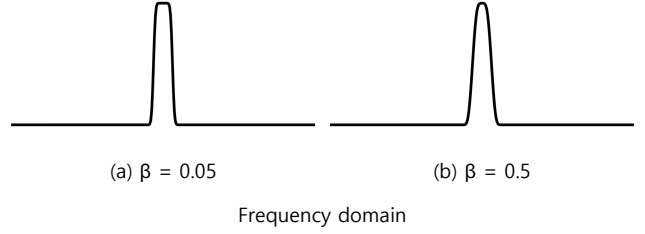


Figure 6: **RC-GAUSS basis function for different cutoff parameters β in the frequency domain.**

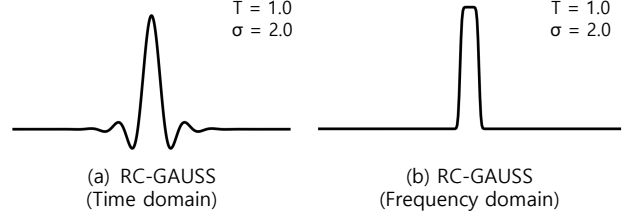


Figure 7: **Joint initialization of T and σ for ideal localization in both domains.**

Task-specific strategy for ζ initialization. In practice, we adopt task-specific initialization strategies for ζ . For image fitting tasks, where the objective is to reconstruct the full-resolution ground-truth image, it is important to accurately represent both low- and high-frequency components to achieve competitive performance with existing models. We find that initializing $\zeta = 1$ consistently yields the best performance, as shown in Table 4, by enabling the model to effectively balance high- and low-frequency components through spectral modulation.

By contrast, restoration tasks such as super-resolution and denoising involve degraded inputs, which typically lack informative high-frequency details due to downsampling or noise corruption. In such cases, a large modulation frequency (e.g., $\zeta = 1$) may overemphasize high-frequency bases, amplifying noise or destabilizing early training. We therefore initialize $\zeta = 0$ to promote low-frequency, smooth basis functions around the DC region, which leads to more stable convergence and improved restoration quality.

B Extended Ablation and Analysis

Visualizing the first-layer neurons to examine the expressiveness of the activation function. To better understand the functional behavior and expressiveness of the activation functions, we visualize the first-layer neurons in a simple image fitting task, as shown in Fig. 9. The figure presents the FFT of FINER (Liu et al. 2024), a SOTA sine-based variable periodic model, and our proposed FLAIR. Unlike FINER, each neuron in FLAIR exhibits clear directional characteristics, suggesting that neurons play distinct, non-redundant roles.

We further assess whether this expressiveness translates into compact yet effective representations by conducting ex-

Table 4: PSNR (dB) results across different values of ζ and training iterations in the image fitting task.

Variable ζ	Iterations		
	1000	3000	5000
$\zeta = 0.0$	18.51	21.31	22.81
$\zeta = 0.5$	28.10	29.62	30.20
$\zeta = 1.0$	30.51	31.31	31.34
$\zeta = 1.5$	25.51	28.57	30.28

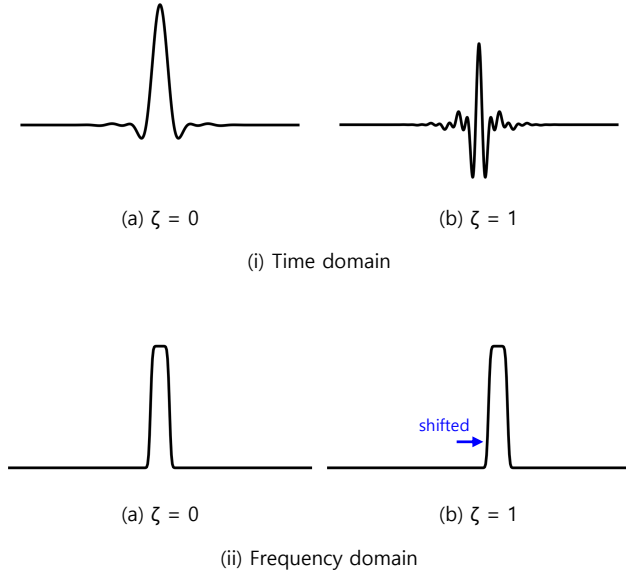


Figure 8: Spectral control via the frequency shift parameter ζ in the RC-GAUSS basis. A larger value of ζ introduces a bias toward representing high-frequency components.

periments under varying numbers of hidden features (64, 128, 256), as shown in Fig. 10. While the performance gap between FINER and FLAIR narrows as the hidden dimension increases, our model consistently outperforms FINER, particularly in perceptual quality (LPIPS), when using fewer hidden features. This highlights the efficiency and compactness of FLAIR’s representation.

Ablation on filtering methods for Wavelet-Energy-Guided Encoding. WEGE provides explicit cues to quantify continuous-frequency components. However, due to its pixel-wise scoring, which causes discontinuity, WEGE can introduce noise into the final RGB output, as seen in the red box of Fig. 11(i)(c). To address this, a score-filtering strategy is required to reduce score discontinuity while preserving edge information. To this end, we evaluate both bilateral and guided filters, as shown in Fig. 11.

As highlighted by the yellow circle in Fig. 11(i), even after filtering, some scores remain noisy compared to their neighboring scores. This results in salt-and-pepper artifacts in the final RGB image, as shown in the red box of Fig. 11(i)(c). While bilateral filtering partially reduces such

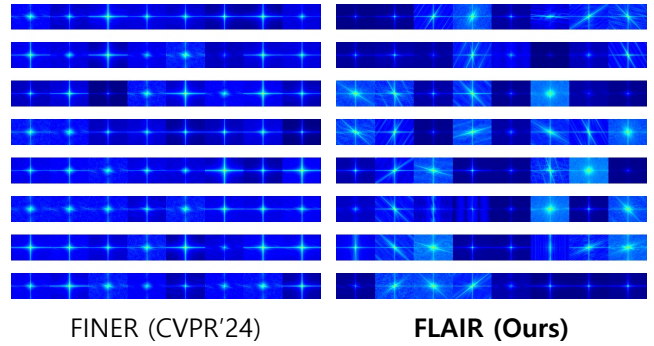


Figure 9: Visualization of FFTs of basis neurons, comparing FLAIR to the SOTA model FINER.

discontinuities, it does not generalize well across scenes. In contrast, guided filtering effectively preserves edges while producing smoother and more consistent score maps, which directly improves performance, as shown in Table 5.

C More Experiment Results

To further validate the effectiveness of our proposed FLAIR, we provide additional experimental results across diverse tasks.

In the fitting task, as shown in Fig. 12, FLAIR accurately reconstructs textures and characters by selecting appropriate frequencies, outperforming other models in fine-detail fitting. For the occupancy task, we evaluate on an additional data not used in the main paper. All models are trained for 500 iterations. As shown in Fig. 13, FLAIR produces more precise geometry with the highest IoU and PSNR scores among all methods.

Lastly, the denoising task serves as an ideal downstream benchmark to assess the model’s ability to appropriately select relevant frequency components. As shown in Fig. 14, while other methods fail to effectively suppress noise, FLAIR demonstrates superior denoising performance by effectively suppressing noise and retaining fine structural details, as shown in the magnified red box.

D Limitations and Discussion

Filter-based activations, due to their sharp cut-off characteristics, behave differently from conventional periodic functions. These activations offer strong advantages in fine-detail representation, but can introduce artifacts such as fragmentation effects in the RGB domain, as shown in Fig. 15.

This may result from inaccurate frequency localization, where the activation attempts to reconstruct fine details even in low-frequency regions. To address this, we incorporated a Gaussian envelope and WEGE to suppress such misaligned responses, though this was not universally effective across all scenes. Future work will explore improved frequency modulation or oscillation control techniques that maintain parameter efficiency and convergence stability.

Ultimately, with the model’s strength in recovering high-frequency details already validated, future research should

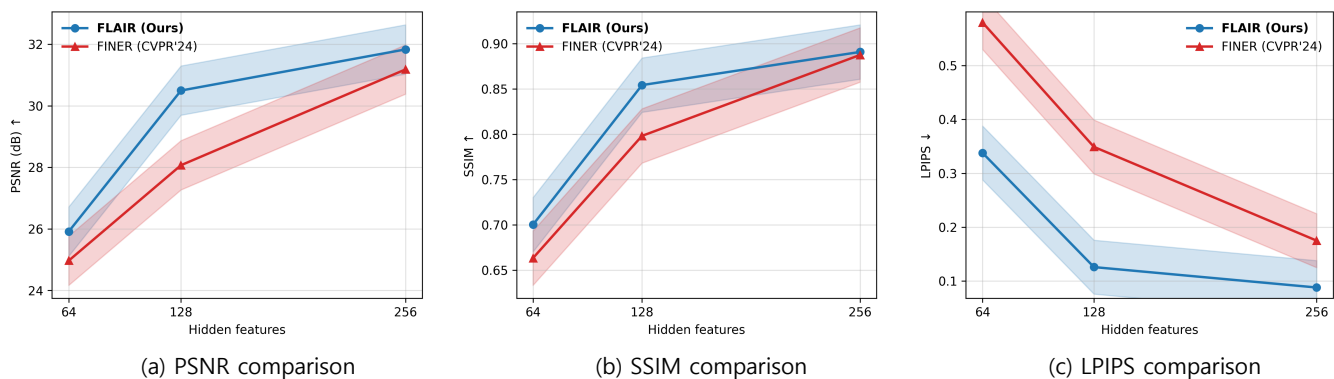


Figure 10: Robustness of FLAIR to the number of hidden features, compared to the SOTA model FINER.

Table 5: Ablation study on WEGE for super-resolution $\times 4$ on DIV2K. Comparison in RG (RC-GAUSS) and FINER pipelines using PSNR (dB), SSIM, and LPIPS. **Bold** denotes the best and underline denotes the second best in each column. Abbreviations: **BF**=Bilateral Filter, **GF**=Guided Filter, **RG**=RC-GAUSS. Designed as a plug-and-play module, WEGE can be integrated with various nonlinear functions. The table shows that it exhibits stronger synergy with RC-GAUSS, and that guided filtering is the most effective in preserving edges without introducing noise.

Method	PSNR \uparrow	SSIM \uparrow	LPIPS \downarrow
w/o WEGE (RG)	26.90	0.7660	0.148
WEGE + BF (RG)	27.06	0.7810	0.137
WEGE + GF (RG)	27.22	0.7960	0.122
w/o WEGE (FINER)	26.80	0.7620	0.152
WEGE + BF (FINER)	26.82	0.7630	0.151
WEGE + GF (FINER)	26.96	0.7760	0.139

pivot toward improving robustness across diverse scenes and minimizing visual artifacts such as fragmentation effects.

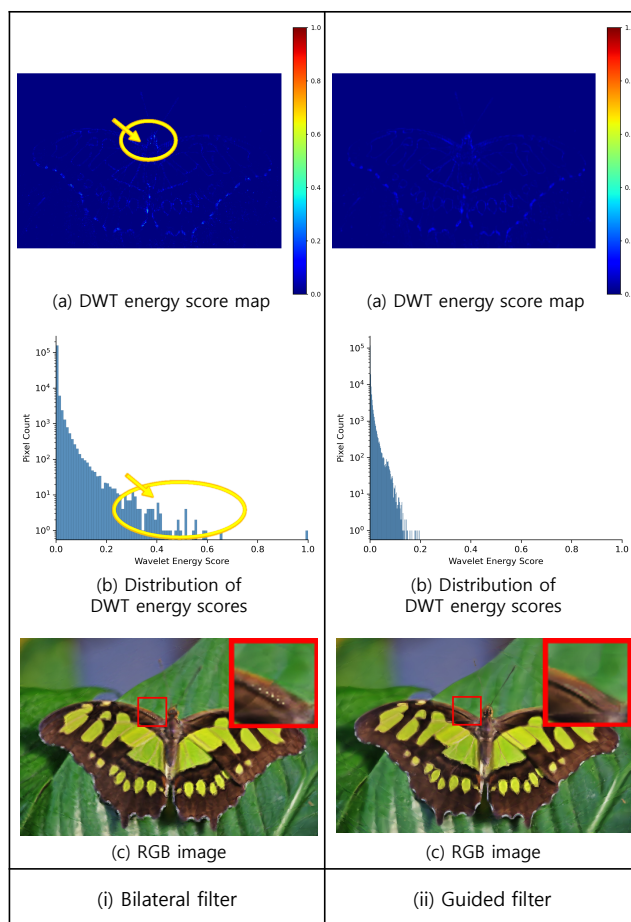


Figure 11: Comparison of filtering methods in WEGE for addressing score discontinuity in DWT energy maps.

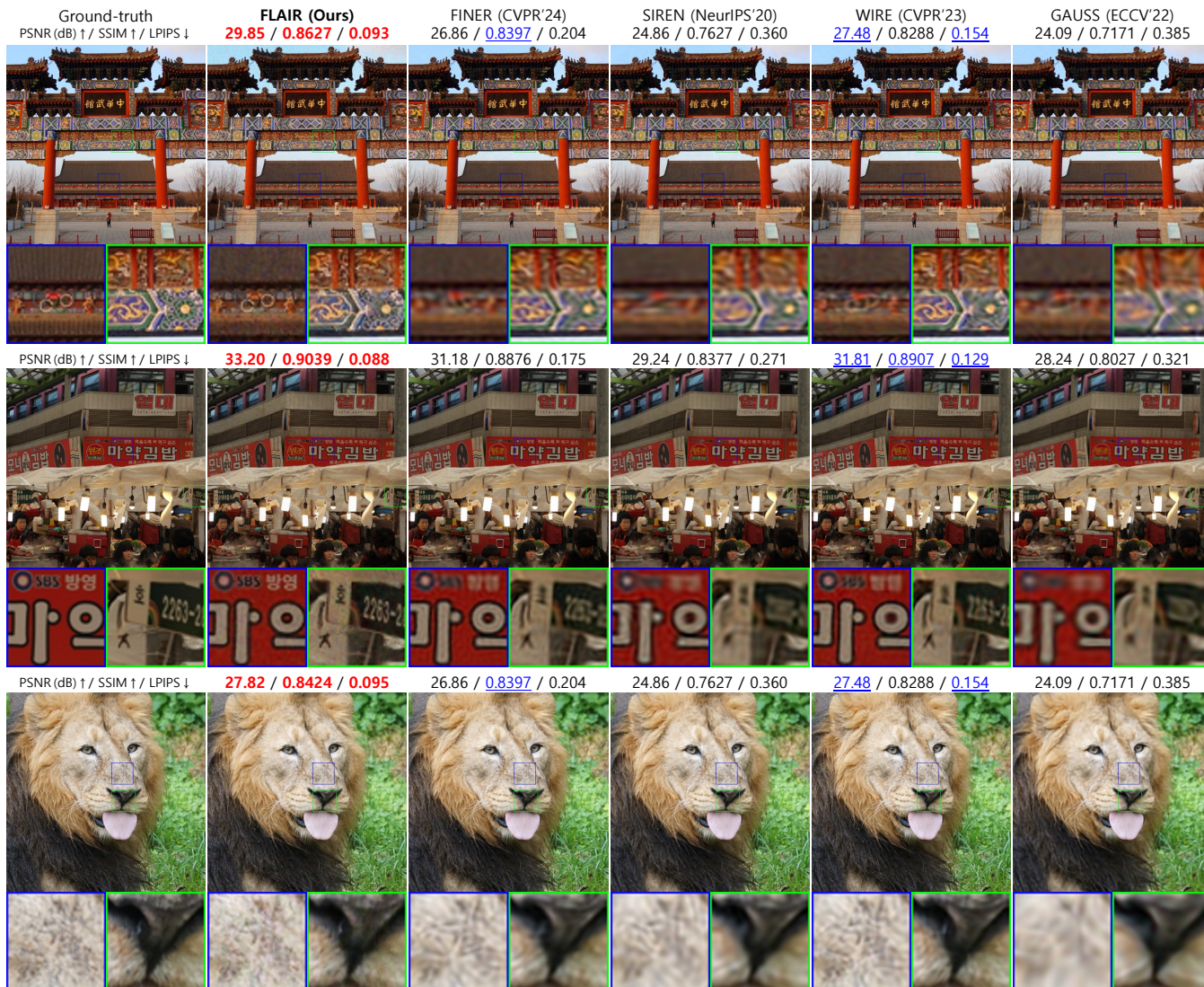


Figure 12: Visual comparisons between FLAIR and baselines on fitting images.

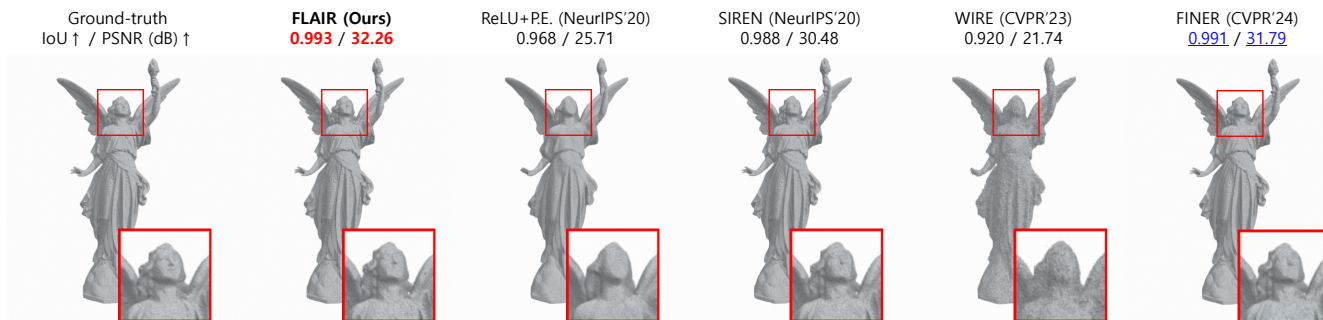


Figure 13: Visual comparisons for occupancy field representations on Lucy data.

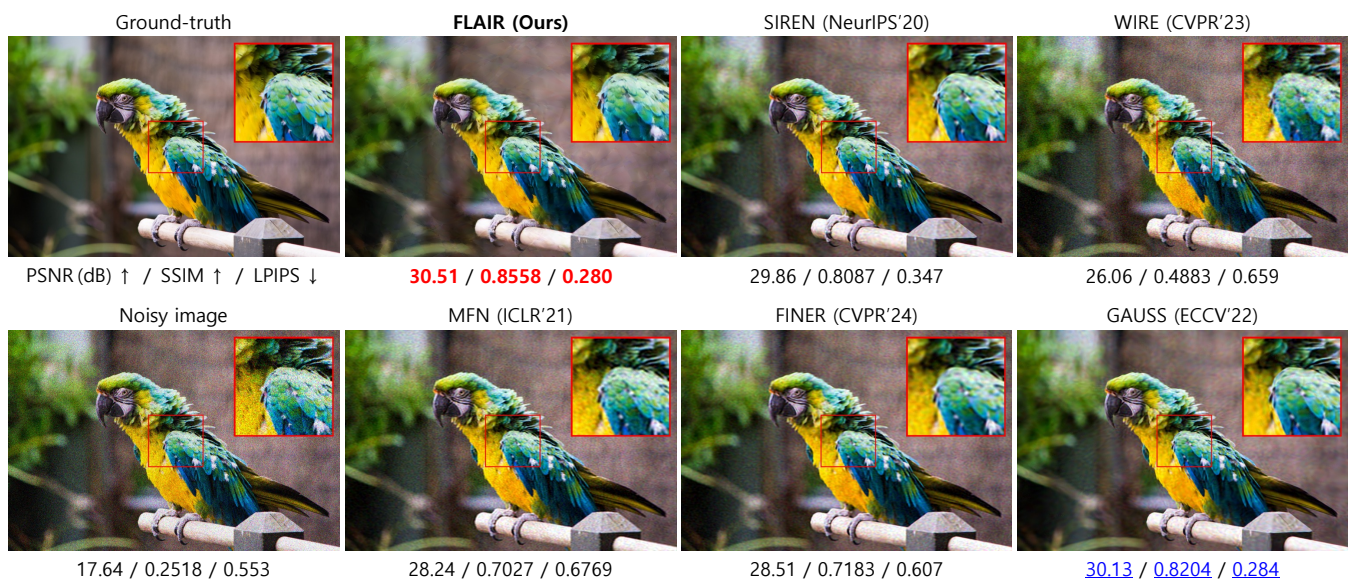


Figure 14: Visual comparisons between FLAIR and baselines on the denoising task.

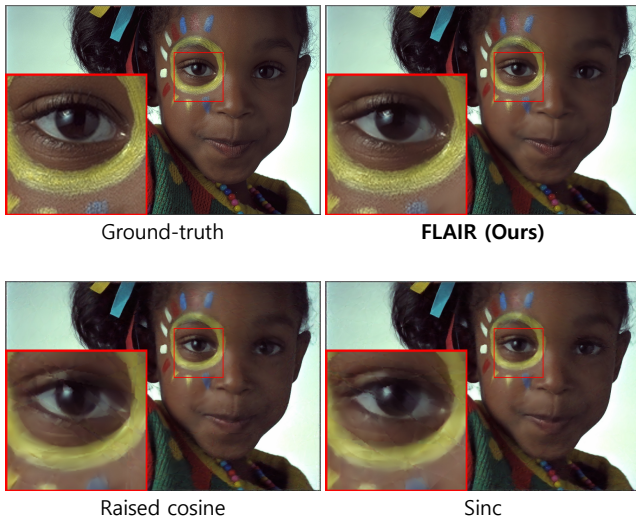


Figure 15: **Visual comparison between FLAIR and other band-limited baselines.** In the fitting task, using the raised cosine or sinc function alone results in visible fragment artifacts in the RGB domain. This artifact occurs when incorrect frequencies are encoded through sharp band-limited activations. In contrast, FLAIR alleviates this issue by leveraging the complementary properties of WEGE and RC-GAUSS.